FLARES AND THEIR UNDERLYING MAGNETIC COMPLEXITY

Alexander J. Engell[1], Marek Siarkowski[2], Magda Gryciuk[2], Janusz Sylwester[2], Barbara Sylwester[2], Leon Golub[1], Kelly Korreck[1], and Jonathan Cirtain[3]
[1] Harvard-Smithsonian Center for Astrophysics, 60 Garden Street, Cambridge MA 02138, USA; aengell@cfa.harvard.edu
[2] Space Research Center, Polish Academy of Sciences, Kopernika 11, 51-622 Wroclaw, Poland
[3] Marshall Space Flight Center NASA, Mail Code: VP62, Marshall Space Flight Center, AL 35812, USA
Received 2010 July 22; accepted 2010 September 9; published 2010 December 9

ABSTRACT

SphinX (Solar PHotometer IN X-rays), a full-disk-integrated spectrometer, observed 137 flare-like/transient events with active region (AR) 11024 being the only AR on disk. The *Hinode* X-Ray Telescope (XRT) and Solar Optical Telescope observe 67 of these events and identified their location from 12:00 UT on July 3 through 24:00 UT 2009 July 7. We find that the predominant mechanisms for flares observed by XRT are (1) flux cancellation and (2) the shearing of underlying magnetic elements. Point- and cusp-like flare morphologies seen by XRT all occur in a magnetic environment where one polarity is impeded by the opposite polarity and vice versa, forcing the flux cancellation process. The shearing is either caused by flux emergence at the center of the AR and separation of polarities along a neutral line or by individual magnetic elements having a rotational motion. Both mechanisms are observed to contribute to single- and multiple-loop flares. We observe that most loop flares occur along a large portion of a polarity inversion line. Point- and cusp-like flares become more infrequent as the AR becomes organized with separation of the positive and negative polarities. SphinX, which allows us to identify when these flares occur, provides us with a statistically significant temperature and emission scaling law for A and B class flares: $EM = 6.1 \times 10^{33} \, T^{1.9 \pm 0.1}$.

Key words: Sun: corona – Sun: flares – Sun: magnetic topology – Sun: photosphere – Sun: X-rays, gamma rays

Online-only material: animations

1. INTRODUCTION

Active region (AR) transient brightenings (Shimizu et al. 1992) or microflares have been observed in X-rays by the Soft X-ray Telescope (SXT; Tsuneta et al. 1991) on board the *Yohkoh* satellite (Ogawara et al. 1991) and the X-Ray Telescope (XRT; Golub et al. 2007) on board the *Hinode* satellite. Transient AR loop brightenings have also been strongly associated with emerging flux regions (EFRs; Yoshimura & Kurokawa 1999; Mein et al. 2001; Kubo et al. 2003; and Seaton et al. 2001). Kurokawa et al. (1994) found that most observed SXT brightenings were located over an EFR.

A chromospheric brightening component in EFRs has been clearly identified in the literature and is known as Ellerman bombs (EBs; Schmieder et al. 2004; Georgoulis et al. 2002). They are identified mostly in the wings of the Hα line. They are not detectable at the Hα line center, implying that they are a feature of either the upper photosphere (Severny 1968) or the low chromosphere (Payne 1993). Brooks et al. (2008) examined chromospheric transient brightenings in an AR without significant flux emergence from the Extreme-UV Imaging Spectrometer (EIS; Culhane 2007) in He II 256.35 Å. The brightenings occur mostly along the main polarity inversion line (PIL) between the two polarities. They find that several instances are due to flux cancellation. They also recognize that not all brightenings are found to be due to flux cancellation. Lastly, the hot loops of EIS Fe XVI 262.94 Å that they examine are located in regions noncontiguous with the opposite polarity interaction and are locally unipolar with no mixed polarity. They suggest that this hot-loop morphology has strong implications for transient versus steady heating of coronal AR loops.

Flux cancellation or canceling magnetic features (CMFs) have been well studied and observationally defined by Livi et al.

(1985) and Martin et al. (1985). Zwaan (1987) suggested that CMFs represent the emergence or submergence of loops due to either magnetic reconnection or simple convective motions, respectively. Kubo et al. (2010) thoroughly study five examples of CMFs in Solar Optical Telescope's (SOT's) spectropolarimetric measurements and *G*-band images. They find that the horizontal magnetic field necessary for both the emergence and submergence of loops is resolved only in one out of the five CMF examples. They conclude that in the remaining four CMF events, the horizontal field is below that of the SOT's resolution at scales less than ∼200 km and close to the solar surface.

Temperature (*T*) and emission measure (EM) comparisons during periods of solar and stellar flaring are well studied (Shibata & Yokoyama 2002; Aschwanden et al. 2008 and references therein). Shibata & Yokoyama (2002) find that the power-law relationships between *T* and EM of these solar and stellar flares can provide us with important parameters on magnetic field strength and loop length that can be further applied to other stellar bodies. More fundamentally, the idea of a single scaling law describing all solar and stellar flares, thereby implying a single mechanism for all, has been long sought (Fisher et al. 1998).

Recently, the SphinX X-ray (Solar PHotometer IN X-rays) spectrometer (Sylwester et al. 2008) on board the *CORONAS-Photon* has observed flaring events over the full disk. SphinX is not able to determine the source locations of these flares but can obtain temperature, EM, and flux diagnostics. Along with the understanding of the magnetic environment as observed by the SOT (Tsuneta et al. 2008), XRT and SphinX together are able to provide a more complete picture of the physical mechanisms that occur during these flares.

This paper investigates the occurrences of transient brightenings, for the remainder of this paper simply called flares,

associated with AR 11024, covering the period 12:00 UT on July 3 through 2009 July 7. We provide an analysis of the physical conditions in these events based on SphinX, XRT, and SOT, with the intention of providing a better understanding of flaring events observed within EFRs.

2. OBSERVATIONS

2.1. Active Region 11024

AR 11024 is of particular interest for a collaborative study among SphinX, XRT, and SOT: (1) it has considerable flux emergence during XRT's observations and is active during its evolution; (2) it is the only AR on disk (even from *STEREO*'s A and B different vantage points) making it easier to isolate and identify XRT's observations of flares associated with SphinX's flare events and other diagnostic counterparts; (3) it is positioned within 45° of disk center during the course of this study, which allows us to more accurately resolve the morphology of the flares without significant projection effects.

There are three main EFRs at the beginning of SOT's observing run on AR 11024. Please refer to the online journal for Animation 1 (xrt_sot_efr_apj.mpeg) that highlights the areas of the EFRs over the course of AR evolution. Two are found to be parallel, with magnetic elements moving in the same directions, while the third EFR (larger of the three initial boxes) emerged with a slight counterclockwise rotation. The photospheric motions caused by these EFRs provide the core of the AR with mixed polarity and complex flows. By July 4 around 23:30 UT the former two EFRs have consolidated and are now seen as nearly one EFR, while the latter EFR has untwisted itself in a clockwise manner to become parallel with the now single EFR. The initial environment and evolution of these three EFRs make for interesting dynamics of the region as magnetic elements are in constant motion. Flux emergence decreases significantly by July 6, 06:00 UT and almost completely by 12:00 UT until a single EFR occurs at the center of the AR on July 7, 09:00 UT. This last identified EFR really starts to become more significant in its emergence around 11:30 on July 7.

2.2. SphinX

SphinX, the Polish X-ray photometer, and spectrometer operated from February 22 to 2009 November 29, aboard Russian satellite *CORONAS-Photon*. SphinX uses three similar PIN detectors (named D1, D2, and D3) equipped with progressively, by a factor of 50, decreasing apertures. The ultimate time resolution of the measurements can be as short as 1 ms. Nominal observed spectral range is between 1.0 keV and 15 keV, resolved electronically into 256 energy bins. SphinX is able to observe the Sun continuously except during eclipse periods (different than XRT's) and transits across the South Atlantic Anomaly (SAA). During the study of AR 11024, eclipses and transits primarily occur on July 3 beginning at 12:55 UT with durations of 10–15 minutes once every 1.5 hr. Eclipse periods and SAA transits continue in the following days with a shorter duration and at a lower frequency. There is only one instance when XRT observes a flare or transient loop brightening when SphinX is unable to observe. This occurred on 2009 July 4 21:41 UT. Otherwise, the eclipse times and SAA transits of SphinX do not impact the joint instrument study.

2.3. XRT

XRT uses the Ti-poly and Be-thin filters during the observation of the AR 11024. The field of view (FOV) is approximately $395'' \times 395''$ (with a pixel scale of $1''.03$). The time cadence of XRT is on average one image every 90 s for each filter during the observing periods. Systematic data gaps last 15–45 minutes occurring once every two hours because of eclipse periods. There are two extended data gaps when XRT observations were paused during eclipse: (1) 2009 July 4 00:00–11:50 UT and (2) 2009 July 6 7:30 UT through 2009 July 7 10:27 UT.

2.4. SOT

SOT's NFI filter observations were used to construct the line-of-sight magnetograms from Stokes V/I. Through July 7 10:46 UT the SOT FOV is only $112''.5 \times 112''.5$ (with a pixel scale of $0''.16$) before changing over to a larger FOV of $225''.3 \times 112''.5$. Despite SOT having slightly more than 1/16 the FOV of XRT's for most of the observational period, it is always centered in the middle of the AR and only misses one flare that XRT observes as it is outside of the SOT FOV. SOT has similar data gaps as XRT due to the *Hinode* eclipses. During initial flux emergence which XRT observes, SOT observes three frames and then has a data gap. The other time which is different than XRT's observations is on July 6. SOT does not experience the extended data gaps as XRT does, only a minor one from 15:53 to 19:52 UT.

2.5. MDI

Using the Michelson Doppler Imager (MDI; Scherrer et al. 1995) as part of the *SOHO* spacecraft (Fleck et al. 1995), 63 magnetograms were obtained to study the magnetic flux during the evolution of AR 11024. The pixel scale is $1''.986$. The magnetograms were taken every 96 minutes during the observation period with one exception of 192 minutes (2009 July 4 00:00–03:12 UT).

3. DATA ANALYSIS

3.1. Data Selection Criteria

We follow a similar set of criteria for selection of flare events in the XRT data to that used by Shimizu et al. (1992) selection of transient coronal brightenings: (1) the AR is at a heliocentric angle less than 45° from the disk center, (2) the image is not saturated to such a degree that the morphological structure cannot be determined, and (3) enough XRT images are obtained to determine whether or not a flare occurred, for comparison with the SphinX flare event.

XRT flares are sometimes more readily identified by analyzing the XRT light curve. We have included Animation 2 (labeled as xrt_sphinx_lc_apj.mpeg) available in the online version of the journal covering a day of XRT and SphinX observations for the reader to see how clearly XRT's and SphinX's light curves follow one another. For XRT images, the data number (DN; integrated pixel value over the whole FOV) is used as the light curve when comparing with SphinX's flare events along with measurements derived from SphinX data. Also, the XRT light curve mirrors the trends of the SphinX light curve very well in both filters. A flare has occurred if the plasma emission increases its intensity rapidly as viewed by XRT or if SphinX has issued a flare event based on its measurements.

3.2. Flare Morphologies

There are 137 SphinX flare events in total during the study. XRT observes 74 of the 137 SphinX flare events. There are four morphological flare types that XRT observes: (1) cusp-like
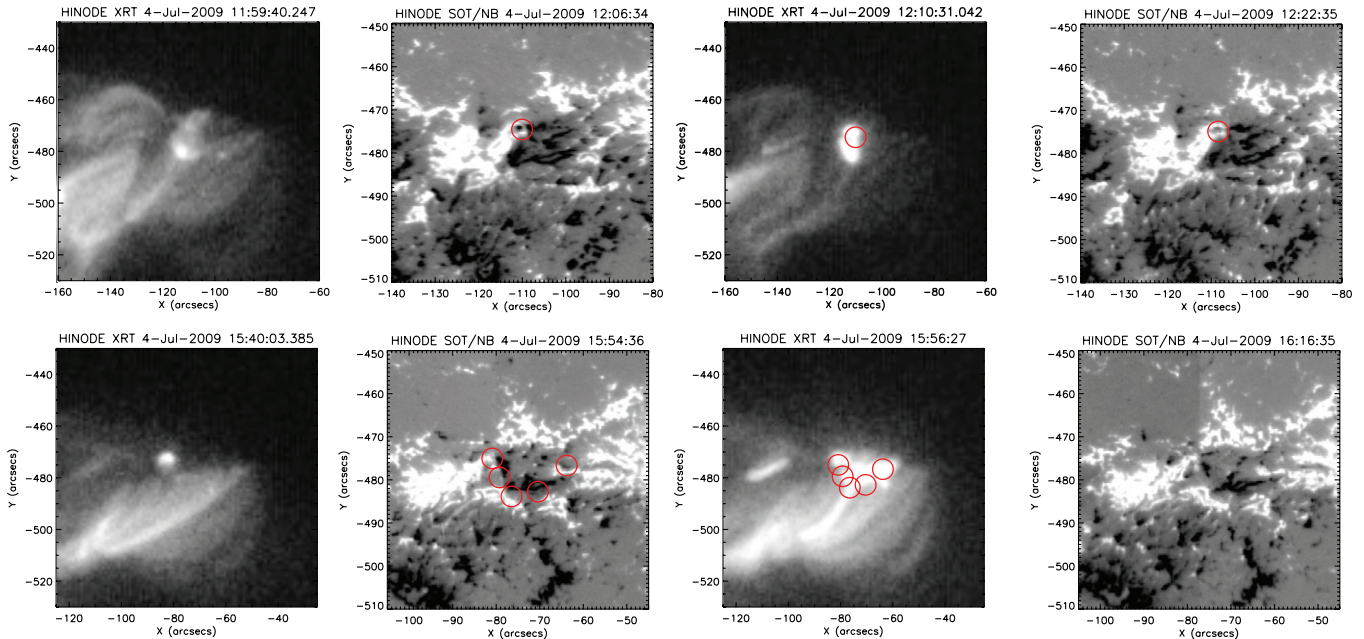
Figure 1. Magnetic cancellation of point and cusp-like flares. The top row illustrates an example of flux cancellation observed in SOT causing a point-like flare in XRT. The bottom row illustrates the same thing but for a cusp-like flare. The location of the red circles is initially chosen where and when XRT observes the flare. They are then overlaid on the SOT magnetograms that illustrate the magnetic flux cancellation the best. For the two SOT magnetograms on the top row, we keep the red circle in the same area to clearly point out the flux cancellation location. We also note that there were several point-like flares during this time. Directly south of the red circle on the top row there is more evidence for flux cancellation that was the cause for other point-like flares during this time period. For the bottom row, notice the almost complete degradation of the black (negative) polarity by the time of the second SOT magnetogram due to the constant flux cancellation.

flare, (2) point-like flare, (3) single-loop flare, and (4) multiple-loop flare. The rightmost images (top and bottom) of Figure 1 show examples of the point-like and cusp-like flares, while the rightmost images (top and bottom) of Figure 2 show the single- and multiple-loop flares.

3.3. SphinX Measurements

For the purpose of the present study, we use the detector D1 signal as it has the largest aperture and, in connection with, substantial count rates, of the order of ~1000 counts s^{-1}, have been observed in the period considered. However, the photons above 3 keV have rarely been recorded, except for the few stronger flares. Detector D1 spectral resolution (0.48 keV) did not allow for easy recognition of individual line groups on the spectra. The SphinX spectra have been recorded over consecutive data gather intervals (DGI) of 1 or 5 s duration. The temperature (T) and EM values characterizing the emitting plasma were calculated based on the measured ratio of fluxes in two selected spectral bands 1.16–1.51 keV and above 1.51 keV, a procedure similar to that commonly used for interpretation of *GOES* X-ray measurements. The isothermal approximation is used in this respect and therefore the values determined represent the average temperature of the flaring plasma. In order to avoid statistical fluctuations, mean values of temperatures as calculated for the period extending 30 s before and after the overall X-ray peak flux (12 values are taken into the average for the 5 s DGI) have been used to characterize the flare. Respective EM values have been determined from the measured lower energy 1.16–1.51 keV band count rates using the calculated temperature response appropriate for detector D1. This temperature response function has been calculated using the CHIANTI v5.2 spectral code and laboratory calibrated energy dependence of detector's effective area. Some details of the SphinX construction can be found in Sylwester et al. (2008).
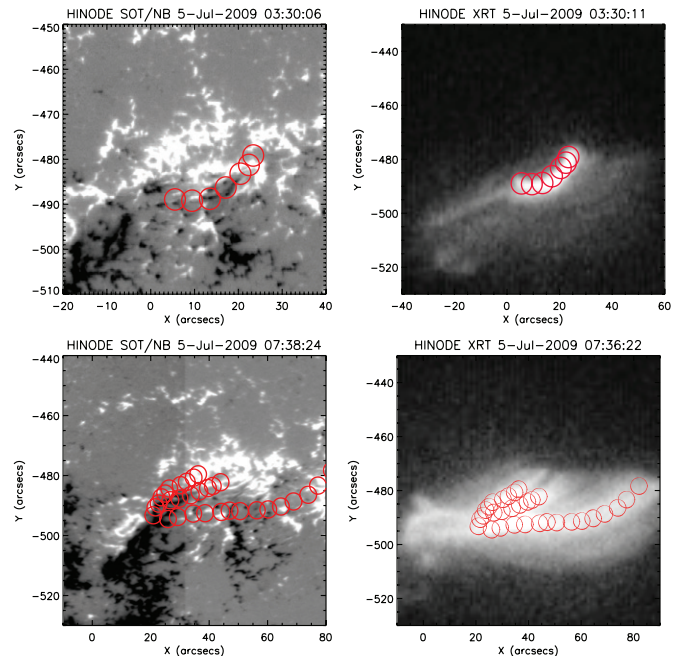

Figure 2. Shearing motions of single- and multiple-loop flares. The top row shows the location of shearing motions from the SOT magnetogram and the corresponding XRT single-loop flare. The bottom row shows the same thing but for a multiple-loop flare. The location of the red circles is initially chosen where and when XRT observes the flare. They are then overlaid on the SOT magnetograms. For the multiple-loop flare, the initial brightening occurred around the red circles furthest to the left (east) and then the three loops observed in XRT brightened shortly after that.

It is important to address the timescales for the peak temperature to be reached in the flares studied in terms of the ion formations. Bremsstrahlung continuum reacts instantly to

3

changed plasma T (as well as line excitations) while it takes time for the ionization fractions to re-adjust. Therefore the line contribution to the spectra may differ from steady state for times necessary for the re-ionization. These timescales are inversely proportional to plasma density and are approximately equal (for Fe XXV) to $10^{12}n_e^{-1}$ [s] (if n_e is per cm^{-3}), so it takes 100 s for the 6.7 keV line group that is dominated by helium-like Fe ion emission to fully appear if plasma density is 10^{10} cm^{-3} and the abrupt T-rise is from 3 to 30 MK. Contribution of the other line groups formed in lower ionization stages of iron or lighter elements will re-adjust more quickly. Using the values of T averaged over 1 minute around flare maximum removes to large extent possible transient bias expected to be the strongest early in the flux rise phase. An adjusted temperature calculation of these early flare phases should be carried out under the transient interpretation. However, this is beyond the scope of this paper.

3.4. Aligning SOT to XRT

There are six main procedures to produce an aligned data set. (1) Align all XRT data to the first known *G*-band image by using xrt_jitter.pro and shift_image.pro. xrt_jitter.pro finds the relative offsets from image to image through the housekeeping of *Hinode*'s orbital variation and XRT's jitter. shift_image.pro makes the shifts to the data set with identified offsets. (2) Align all SOT data to the same time as the XRT *G*-band image by using align_cube_correl.pro which aligns all SOT images to that time via cross-correlation. (3) Use the procedure im2xrt_sot_offsets to get the DC offsets between XRT and SOT at the time of the *G*-band image. (4) Using the two offset arrays from both XRT and SOT you can correct the XCEN and YCEN pointing keywords for both XRT and SOT. (5) We then adjust SOT's XCEN and YCEN pointing keywords by the DC offsets. (6) Once the XRT and SOT data set is put into a map array, they are aligned within residual errors. Based on the flux cancellation sites, the residual errors were found to be $2''$–$4''$. This is roughly the diameter of the red circles drawn in Figures 1 and 2.

3.5. Measuring MDI Flux

We use MDI to calculate the total unsigned flux of AR 11024 because the AR is larger than the SOT's FOV. From the full-disk MDI magnetograms, a subarea was selected to measure the flux in AR 11024. When it is projected into Cartesian coordinates this subarea results in the same $200'' \times 200''$ area for all 63 magnetograms used. This is done to provide the most accurate flux measurement. The selection subarea size did not change over the course of the four-day observing time. For the purpose of this study, only the total unsigned flux is used so any magnetic ambiguity within the AR is not of concern.

4. RESULTS

4.1. XRT and SphinX Observe the Same Flaring Events

The synchronous evolution of the XRT and SphinX light curves illustrates that the two instruments observe the same or very similar physical processes in the solar corona. The peak times of SphinX flare events coincide with either loop brightenings (single- and multiple-loop flares) or cusp- and point-like flares. The lack of other AR on the Sun significantly reduces any chances of flares outside of XRT's FOV coinciding with that of the SphinX flare events. We are therefore confident that both instruments observe the same unique event.

4.2. Flux Cancellation

XRT observes 19 cusp- and point-like flares. Of these, 12 occur within SOT's FOV and observing time. Examining these 12 flares by selecting the region of the flare in XRT and overplotting the region on the SOT magnetogram as illustrated in Figure 1, we find that 11 of these flares (92%) are directly associated with flux cancellation. In addition to Figure 1, we include Animation 3 (xrt_sot_flares_apj.mpeg) in the online version of the journal that overlays red circles (flares that are identified on XRT images) on to the SOT magnetograms. In this animation, the red circles mark the location where XRT observes the flare. In many instances, there is magnetic cancellation directly responsible for the flares observed by XRT, especially in the early stage of AR evolution when magnetic elements are unorganized. The main observational circumstance for all of these observed flux cancellations is that one or both polarities have a direct photospheric motion toward each other and any continuation of a polarity's motion is impeded by the other's location. Magnetic elements of both polarities appear to combine with other like polarities by an overall shearing motion that is a consequence of Joy's law. In all 12 instances, due to these impediments resulting from photospheric motions and of the locations of the EFRs, we attribute forced flux cancellation as the cause for 11 of the point- and cusp-like flares as seen in the X-rays. We also find two single-loop flares occurring as a result of this type of forced flux cancellation. For the other single- and multiple-loop flares the specific role of flux cancellation is unclear.

4.3. Shearing Motions

The single- and multiple-loop flares make up the remaining 55 flares that XRT observed. SOT does not miss any of the single- or multiple-loop observations. Although we can only determine flux cancellation as the cause for loop flares in two cases, the photospheric shearing motions observed in the SOT along with the magnetic sheared loops observed by XRT strongly implies that the cause is dominated by the shearing motions (see Figure 2 and Animation 3 (xrt_sot_flares_apj.mpeg) available through the online journal), resulting in magnetic reconnection, and then likely submergence of flux at the photosphere (another process that results in flux cancellation; van Ballegooijen & Martens 1989). Most flare loops in this study occur along a portion of the PIL as seen in the online animation. In several cases, loop footpoints brighten before brightening of the entire loop (which is marked as the peak of the flare by SphinX).

4.4. Flare Morphologies and Their Respective Temperatures

In Table 1, the flares observed by XRT are classified by morphology, along with corresponding temperature values found by SphinX. We find that cusp- and point-like flares have the same mean temperatures of 11.8 MK. Single-loop flares are lower at 11.2 MK followed by multiple-loop flares at 10.6 MK. Due to the standard deviations of these values they are all essentially comparable in nature.

4.5. Temporal Distribution of Flare Morphologies during AR Evolution

Figure 3 plots all 137 flares observed by SphinX with the corresponding peak flare temperatures (right *y*-axis). Symbols other than crosses represent XRT flare types associated with the SphinX flare events. Starting on 2009 July 3 20:14 UT through
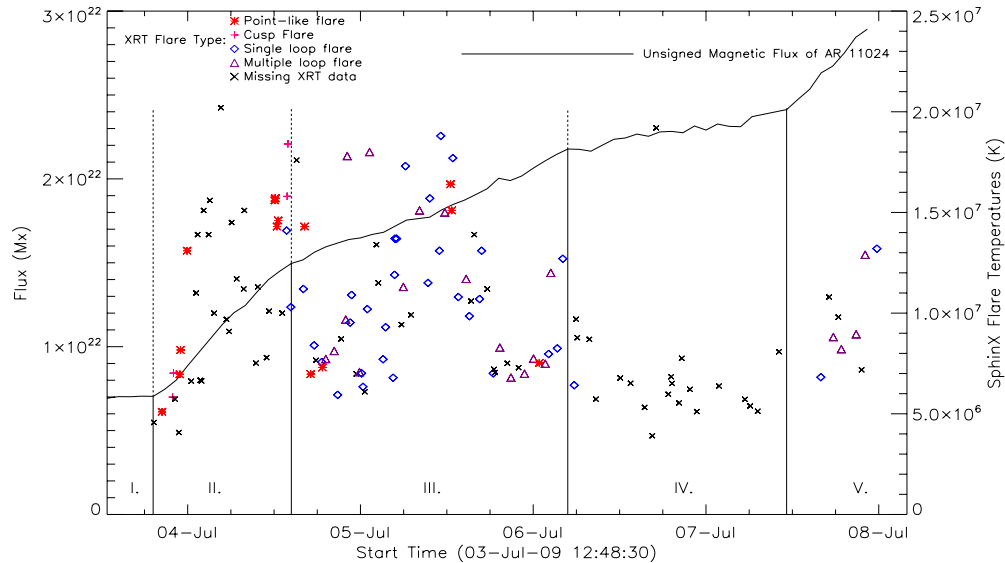
Figure 3. Distribution of XRT flare morphologies along with all SphinX flare events at different stages of evolution in AR 11024. The vertical lines split the evolution of AR 11024 into stages determined by alterations in the rate of change of the total unsigned magnetic flux which is the trending black line. The left y-axis measures the total unsigned flux in the region and the right y-axis denotes the temperature of the flare calculated from SphinX. Each plotted symbol indicates either the XRT flare morphology or represents missing XRT data ($\times$).

Table 1
XRT Flare Statistics

XRT Flare Morphology	Number of Events	% (Total = 74)	Mean Temp (MK)	σ^{a} (MK)
Cusp	4	5.0	11.8	6.3
Point-like	15	20.3	11.8	4.2
Multiple loop	21	29.4	10.6	3.5
Single loop	34	45.9	11.2	4.8

Note. [a] σ represents the relative dispersion of measured temperature within each flare morphology.

July 4 17:06 UT (marked as the flux emergence stage II in Figure 3), SphinX observes 38 flare events. XRT takes data during 15 of these events and 13 are identified as either cusp- (four in total) or point-like (nine in total) flares. There are two single-loop flare types identified by XRT and no multiple-loop flares observed within the 38 SphinX flare events. Prior to the two single-loop flares that occur at the very end of flux emergence stage II, the AR hosts a poor loop environment. We see that one footpoint of the single-loop flares is rooted in the environment where the point- and cusp-like flares have dominated due to the flux cancellation. We attribute the cause of these two single-loop flares to flux cancellation just as all point- and cusp-like flares were. Therefore, all observed flares in stage II flux emergence are due to flux cancellations.

Out of the remaining 99 SphinX flare events, post July 4 17:06 UT, XRT observes during 59 of them. Fifty-three of the 59 are determined to have either single- (21 in total) or multiple-loop (34 in total) flare morphologies. The loop flares generally form by way of an initial footpoint brightening which then brightens the entirety of the loop whether it was visible before or not. However, we could only find two of these flares that were a direct consequence of flux cancellation. During the first few single- and multiple-loop flares, XRT observes that the AR develops an environment of loops. Some loops also remain present outside the areas of flares with lower intensities. The remaining six flares are all point-like flares.

4.6. Temperature and Emission Measure of the SphinX Flares

Figure 4 provides the temperature and EM relationship for all 137 flares that SphinX observes. The distribution of flares in terms of the *GOES* and SphinX classification (which extends the *GOES* classification to flares of lower fluxes due to its superior sensitivity) is as follows: 3 C class flares, 71 B class flares, 61 A class flares, 1 s class flare, and 1 Q class flare. s class covers a range of equivalent $GOES_{1-8}$ Å band fluxes from 10–8 to 10–9 W m^{-2} and Q from 10^{-9} to 10^{-10} W m^{-2}. We find EM = $6.1 \times 10^{33} T^{1.9 \pm 0.1}$. Error bars are plotted in Figure 4. They decrease in magnitude for the larger flares. This is because those flares have a higher count rate hence better statistics due to the higher photon counting within the data gathering intervals.

4.7. Flux Emergence and Flare Rate

In Figure 3, the thick black line trending from the bottom left to the top right is the total unsigned flux. This is calculated by measuring the flux through subareas of 63 MDI magnetograms, containing the magnetic flux associated with AR 11024 (as explained in Section 3.5). Examining the trend of the unsigned flux suggests that there are five flux emergence stages. The vertical lines are positioned at the time of a flux stage change. Stage I has a very low amount of flux increase with a flux rate of 1.72×10^{19} Mx hr^{-1}. There are no flare events observed by SphinX or in the XRTs FOV during the 6.4 hr duration of stage I. The last flare event recorded by SphinX prior to this flare study was on 2009 July 2 and is unlikely associated with AR 11024 as XRT observed it as a large bright point with no sign of activity during the SphinX flare time.

Table 2 shows the breakdown of properties within each flux stage. From stage I to stage II, we observe almost a 25-fold increase in the flux emergence rate to 4.13×10^{20} Mx hr^{-1} along with the first flares associated with AR 11024 at a rate of 1.92 flares hr^{-1}. The flux rate in stage III drops to 1.78×10^{20} Mx hr^{-1} with a flare rate of 1.80 flares hr^{-1}. Stage IV has the lowest flux emergence rate out of all the stages with value 7.73×10^{19} Mx hr^{-1} not including stage I. Its corresponding low flare rate is 0.71 flares hr^{-1}. Stage V has the highest flux
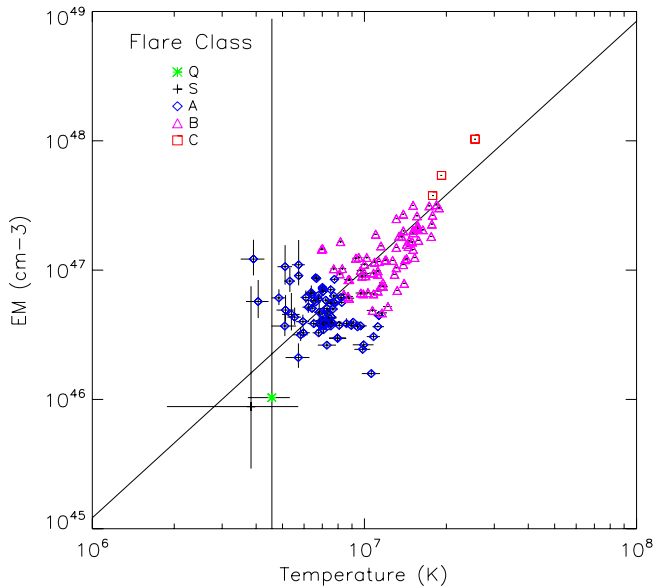
Figure 4. SphinX's T vs. EM. Plotted are the 137 flares observed by SphinX. The separate colors and symbols represent the different classes of flares observed (see the legend in the plot). The error bars in both x (temperature) and y (emission measure) are plotted and decrease as the flares increase in class. This is due to the fact that the higher class of flares has better statistics. The black diagonal line trending from the bottom left to the top right is the best-fit line for the T and EM scaling law: EM $= 6.1 \times 10^{33} T^{1.9\pm0.1}$.

Flux Stage	Duration (hr)	Flux Rate (Mx hr^{-1})	Flare Rate (flares hr^{-1})
I	6.4	1.72×10^{19}	0
II	19.75	4.13×10^{20}	1.92
III	37.75	1.78×10^{20}	1.80
IV	31	7.73×10^{19}	0.71
V	12.5	4.28×10^{20}	0.72

that there are different EFR environments. It is the combination of these that results in the different stages of flare activity. Initially, in SOT observations at 12:00 UT on July 4, there are three clearly noticeable locations of EFRs. There are rotational aspects as well as channels of diverging magnetic element flow. These are likely driven at the photosphere and by the underlying convective zone supplying the AR with many different kinds of magnetic interactions; most noticeably flux cancellation and strong evidence of photospheric shearing. These processes occur during all of stage II when the AR is young and the highest flare rate is observed. For stage V, despite the comparatively high flux rate without a similar flare rate as in stage II, we recognize that there is only a single EFR. By itself, this single EFR is likely to be the cause of the majority of the nine flares as observed in stage V. Yet without the additive complications of other separate EFRs, it is not surprising that the flare rate is not more comparable to stage II.

Of the 142 transient brightenings studied by Shimizu et al. (1994), 18.3% were point-like, 41.5% were single-loop, and 40.2% showed multiple-loop morphologies. We obtain similar percentages for point-like and single-loop flares at 20.3% and 45.9%, respectively, for the 64 flares XRT observes. We find that multiple-loop flares occur 29.4% of the time. This is $\approx 2\sigma$ less than Shimizu et al. (1994) multiple-loop transient brightenings, which may be due to AR 11024 being morphologically less complicated than that of AR 6891 from the Shimizu et al. (1994) study. They report no evidence of cusp-like flares or any other flare morphology that can be described by that name, while cusp-like flares account for 11.8% of XRT's observed flares in this study. SXT was likely not able to resolve these cusp-like flares due to its lower resolution. Higher resolution in the X-rays is key to further understanding not only coronal structure but also the relationship between the dynamics of the photosphere and corona. As this paper demonstrates XRT and SOT can achieve this and the two instruments should be further utilized for such studies.

Because the distribution of XRT flare types in AR 11024 provides strong evidence that cusp- and point-like flares dominate during the initial stage of flux emergence (II), it is important to consider distributions of flare morphologies within each stage. In stage II, all XRT flare morphologies are cusp- or point-like except for two single-loop flares (see Figure 3). After this, single- and multiple-loop flares are observed to dominate the remaining flare activity with the development of a loop environment in AR 11024. We identify initial footpoint brightenings that are observed prior to single- and multiple-loop flares. These are due to X-ray emission from chromospheric or low-temperature coronal matter present around the bases of the coronal loop (Shimizu et al. 1992).

emergence rate of 4.28×10^{20} Mx hr^{-1}, but the flare rate is only 0.72 flares per hour.

5. INTERPRETATION AND CONCLUSIONS

We have observed several aspects of an emerging AR focusing on the properties of the flares and the magnetic environment from where they were produced. From the observations, we identify relationships between the photospheric motions, X-ray coronal component, and diagnostic measurements of EM and T during X-ray flares.

5.1. Flares (Transient Brightenings)

Shimizu et al. (1992) studied "transient coronal brightenings" using *Yohkoh* SXT. Considering the similar morphologies between this present flare study and their transient coronal brightenings study, they may be classified as the same type of events. Shimizu et al. (1992) found that transient brightenings occur with the rate of one every ≈ 3 minutes in "active" ARs to one every ≈ 1 hr in "quieter" ARs. In our study, the highest flare rate during any stage for AR 11024 is 1.92 flares hr^{-1} making it two times more active than "quieter" ARs. The last two stages (IV and V) of AR 11024 during the study have a flare rate well below the "quieter" AR classification reported by Shimizu et al. (1992).

Although the relationship between the flux emergence rate and flare rate is not linear, it follows a trend: if the flux emergence rate increases from the previous stage, then the flare rate also increases; if the flux emergence rate decreases from the previous stage, then the flare rate also decreases. This strongly agrees with many previous works that flux emergence is a main driver of flares. However, stages II had V have similar flux emergence rates; yet stage V has a much lower flare rate than stage II (0.72 versus 1.92 flares hr^{-1}).

In order to address this, we recognize that the flare study of AR 11024 reveals in addition to the stages of flux emergence

5.2. Photospheric Motions

AR 11024 has similar flux emergence to previous studies that focused on the relationship between flux emergence and

EBs (Georgoulis et al. 2002; Schmieder et al. 2004). Schmieder et al. (2004) found that bright moss regions where EBs occurred were also found to be the location where SXT loops were rooted as well as where they brightened. Identifying the flux cancellation of 11 out of 12 cusp- and point-like flares in this study and referring to Figure 3(a) from Georgoulis et al. (2002), we see that the site of strong converging magnetic elements is an environment that hosts both EBs and X-ray cusp- and point-like flares. Although they do not specifically state flux cancellation as the cause for the EBs and only note the convergence of opposite polarities, we suggest that flux cancellation is very likely. Since we observe cusp- and point-like flares originating from magnetically similar environments, we suggest that these two flare morphologies share the same physical mechanism for flare onset, namely forced flux cancellation via magnetic convergence.

Both Brooks et al. (2008) and Kubo et al. (2010) identified examples of flux cancellation in non-EFRs. Despite this, we recognize that the causes for such cancellations may be shared between our study and theirs. Brooks et al. (2008) find similar chromospheric brightenings response to that of EBs, but instead of Hα it is He II 256.35 Å where some are noted to be due to flux cancellation. As posed by Kubo et al. (2010), the reason in their study for only finding one out of the five flux canceling polarities close to the moat of a sunspot having a horizontal magnetic field is due to that it occurs at a scale $\sim$200 km which is below the resolution of the SOT. For flux cancellation without the observation of horizontal magnetic field, they suggest that there is a mergence of polarities due to the converging and downward flows (see Figure 7, panel (a) of Kubo et al. 2010). This is similar to Figure 3(a) from Georgoulis et al. (2002) but now with the inclusion of downflows. From our study, we emphasize the necessity on having an environment that forces the flux cancellations and that when an AR has complex EFRs there are likely to be such environments.

Brooks et al. (2008) examine EIS Fe XVI 262.94 Å which identifies a hot loop. Fe XVI is similar to XRT's Ti-poly and Be-thin filters used in this study. They state that hot loops like these are located in areas away from the opposite polarity interaction. In Figure 5 from Brooks et al. (2008), they identify a hot loop that is clearly rooted in such an area. However, in the same figure that they provide, there is a brighter (hotter) loop nearby that has one footpoint located roughly at the PIL, in a mixed-polarity areas. In this study, we find that a majority of hot loops form through flaring in such mixed-polarity areas. Moreover, Schmieder et al. (2004) find that hot loops (as observed by the SXT) are seen to brighten in the same areas as EBs, which are observed to occur in places of mixed polarity. They note that cooler *TRACE* loops were heated at their footpoints, while SXT loops are heated due to magnetic reconnection. This is not say that SXT loops are not heated at their footpoints due to reconnection. In fact, as shown in Figure 2, in our study we observed many single- and multiple-loop flares that seem to be associated with footpoint reconnection, as was observed in Shimizu et al. (1992).

The majority of loops were left helical (both flaring and non-flaring) in XRT during the course of this study. The observed photospheric shearing with positive moving westward (right) and negative polarities moving eastward (left) gives the underlying reason for this observed magnetic shear. We find two instances where loop flares are caused by direct flux cancellation at one footpoint. Moreover, we recognize that the majority of loop flares occur along a PIL that has shearing motion, as in

Figure 2. We argue that the flaring or brightenings of loops can come through either forced flux cancellation by opposite polarity impediment or by the shearing (potentially a type flux cancellation) of the underlying photospheric polarity elements. This is quite consistent with the behavior shown in Figure 1 from van Ballegooijen & Martens (1989), which describes flux cancellation in a shearing magnetic field due to photospheric flows. They indicate that the shearing may produce a helical loop through further reconnection. Noticing that the photospheric flows are not purely acting in a linear shearing motion but in an often curved shearing motion (top of Figure 2) explains not only the sheared XRT flare loops but also the curvature that is associated with many of the loop flares. We do observe some hot XRT loops rooted in areas of unmixed polarity, but those are not the brightest loops and are also the non-flaring loops. We hypothesize that they may have formed through a more slowly shearing motion not at the core of the AR.

5.3. T–EM Scaling Law

We find a *T*–EM scaling law for 137 solar flares with a power-law slope of $\sim$2. This is much smaller than that of previous studies of solar and stellar flares. Aschwanden et al. (2008) find the power-law slope to be on the order of $\sim$4.0 and $\sim$4.7 for solar + *RHESSI* and solar flares, respectively. For the scaling laws including *RHESSI* data, there is a systematic bias that *RHESSI* determines higher temperature, i.e., $T_{RHESSI} \approx 1.31 T_{GOES} + 3.12$ [MK] (Battaglia et al. 2005). The values of *T* and EM as determined from SphinX spectra under isothermal approximation are expected to be close to the actual maximum plasma temperatures owing to the form of the energy response of the SphinX instrument. The plotted symbols from Figure 4 nicely fall inside the box for AR brightenings (Shimizu 1995) and the group of *RHESSI* points (Battaglia et al. 2005) presented by Aschwanden et al. (2008). Ashwanden also reported the EM $\approx T^{4.0}$ relation for these and other solar instruments interpreted using the isothermal assumption. Such EM $\approx T^{4.0}$ relation is characteristic for the so-called quasi-steady state dependence (Jakimiec et al. 1992).

The inclination characteristic for SphinX point shown in Figure 4, i.e., EM $\approx T^{1.9}$, is much flatter which may be indicative for a specific character of plasma conditions within the studied AR brightenings. Given the high resolution and unprecedented sensitivity of SphinX along with the large number (137) of flares included in our study, we have presented a representative *T*–EM scale law for A and B class flares observed during the period of prolonged minimum of solar activity. For a future study, we will investigate *RHESSI* observations and compare them to that of SphinX's.

REFERENCES

Aschwanden, M. J., Stern, R. A., & Güdel, M. 2008, ApJ, 672, 659
Battaglia, M., Grigis, P. C., & Benz, A. O. 2005, A&A, 439, 737
Brooks, D. H., Ugarte-Urra, I., & Warren, H. P. 2008, ApJ, 689, L77
Culhane, J. L. 2007, in ASP Conf. Ser. 369, in New Solar Physics with Solar-B Mission, ed. K. Shibata, S. Nagata, & T. Sakurai (San Francisco, CA: ASP), 3
Fisher, G. H., Longcope, D. W., Metcalf, T. R., & Pevtsov, A. A. 1998, ApJ, 508, 885
Fleck, B., Domingo, V., & Poland, A. I. 1995, Sol. Phys., 162, 1
Georgoulis, M. K., Rust, D. M., Bernasconi, P. N., & Schmieder, B. 2002, in Proc. Magnetic Coupling of the Solar Atmosphere Euroconference, ed. H. Sawaya-Lacoste (ESA Special Publication, Vol. 505, SOLMAG 2002; Noordwijk: ESA), 125
Golub, L., et al. 2007, Sol. Phys., 243, 63
Jakimiec, J., Sylwester, B., Sylwester, J., Serio, S., Peres, G., & Reale, F. 1992, A&A, 253, 269
Kubo, M., Low, B. C., & Lites, B. W. 2010, ApJ, 712, 1321
Kubo, M., Shimizu, T., & Lites, B. W. 2003, ApJ, 595, 465
Kurokawa, H., Kawai, G., Tsuneta, S., & Ogawara, Y. 1994, in X-ray Solar Physics from Yohkoh, ed. Y. Uchida, T. Watanabe, K. Shibata, & H. S. Hudson (Japan: Universal Academy Press), 59
Livi, S. H. B., Wang, J., & Martin, S. F. 1985, Aust. J. Phys., 38, 855
Martin, S. F., Livi, S. H. B., & Wang, J. 1985, MPA Rep., 212, 179
Mein, N., Schmieder, B., DeLuca, E. E., Heinzel, P., Mein, P., Malherbe, J. M., & Staiger, J. 2001, ApJ, 556, 438
Ogawara, Y., Takano, T., Kato, T., Kosugi, T., Tsuneta, S., Watanabe, T., Kondo, I., & Uchida, Y. 1991, Sol. Phys., 136, 1
Payne, T. E. W. 1993, BAAS, 25, 1395
Scherrer, P. H., et al. 1995, Sol. Phys., 162, 129
Schmieder, B., Démoulin, P., Rust, D. M., Georgoulis, M. K., & Bernasconi, P. N. 2004, in IAU Symp. 219, Stars as Suns: Activity, Evolution and Planets, ed. A. K. Dupree & A. O. Benz (San Francisco, CA: ASP), 483
Seaton, D. B., Winebarger, A. R., DeLuca, E. E., Golub, L., Reeves, K. K., & Gallagher, P. T. 2001, ApJ, 563, L173
Severny, A. B. 1968, in Mass Motions in Solar Flares and Related Phenomena, ed. Y. Oehman (New York: Wiley), 71
Shibata, K., & Yokoyama, T. 2002, ApJ, 577, 422
Shimizu, T. 1995, PASJ, 47, 251
Shimizu, T., Tsuneta, S., Acton, L. W., Lemen, J. R., Ogawara, Y., & Uchida, Y. 1994, ApJ, 422, 906
Shimizu, T., Tsuneta, S., Acton, L. W., Lemen, J. R., & Uchida, Y. 1992, PASJ, 44, L147
Sylwester, J., Kuzin, S., Kotov, Y. D., Farnik, F., & Reale, F. 2008, J. Astrophys. Astron., 29, 339
Tsuneta, S., et al. 1991, Sol. Phys., 136, 37
Tsuneta, S., et al. 2008, Sol. Phys., 249, 167
van Ballegooijen, A. A., & Martens, P. C. H. 1989, ApJ, 343, 971
Yoshimura, K., & Kurokawa, H. 1999, ApJ, 517, 964
Zwaan, C. 1987, ARA&A, 25, 83